A Cyclone Flow Cell for Quantitative Analysis of Kinetics at Porous Electrodes by Differential Electrochemical Mass Spectrometry

F. Kubannek, U. Krewer*

Institute of Energy and Process Systems Engineering, Technische Universität Braunschweig, Franz-Liszt-Str. 35, Braunschweig, Germany

ARTICLE INFO

Keywords:
Differential Electrochemical Mass Spectrometry (DEMS)
Reaction kinetics
Porous electrodes
Cyclone flow
CO oxidation

ABSTRACT

In this work the scope of differential electrochemical mass spectrometry (DEMS) is extended towards quantitatively identifying kinetics of electrochemical reactions in porous electrodes by dynamic measurements. The method is demonstrated by analyzing the kinetics of CO oxidation on a carbon supported Pt/Ru catalyst using a cyclone flow DEMS cell, which allows online studies of porous electrodes. The cyclone flow cell generates a rotating flow field above the stationary electrode. Experimentally validated CFD simulations show that the constructed cell features a homogeneous concentration boundary layer over approximately 75% of the electrode surface area, and that the diffusion limited current density is proportional to flow rate to the power of two third, which is characteristic for turbulent flows. Calibration experiments are performed, and a physical model including mass transfer and reactions inside the porous electrode as well as information about the concentration boundary layer from the CFD results is set up. By matching simulation results and experimental data for CO oxidation, kinetic parameters are determined. With DEMS, not only current and potential but also the CO_2 production rate can be observed with a high time resolution which allows to conduct quantitative macrokinetic analysis and to identify parameters quite reliably with a low number of dynamic experiments.

1. Introduction

Differential Electrochemical Mass Spectrometry (DEMS) is a powerful technique for analyzing volatile products and intermediates of electrochemical reactions online and directly at the electrode. First cells were designed by Wolter and Heitbaum [1] who deposited a porous electrode directly on a porous teflon membrane through which reaction products could enter a differentially pumped vacuum chamber and, subsequently, be detected by the mass spectrometer within approximately 0.1 seconds. Since DEMS is a quantitative technique and volatile species can be detected with an extremely short delay time, it seems highly suitable for analyzing reaction kinetics and dynamic processes.

The performance of a DEMS device, however, strongly depends on the cell design which has to be adopted to the desired application. Therefore, numerous electrochemical DEMS cells have been designed for the purpose of solving specific scientific problems.

Since there is no convection in the classical DEMS cells, the mass transfer is not well-defined making it difficult to analyze concentration dependent adsorption and reaction processes that play an important role in technical electrodes. Fujihira and coworkers [2] included a rotating rod above the working electrode to increase mass transport. Wasmus and coworkers [3] used a rotating porous electrode which they placed near to the PTFE membrane. This approach led to increased convection but the flow was still not well-defined and only a small fraction of the products was transported through the solution and the membrane into the vacuum system. Another approach for generating defined convection is to use a rotating inlet system resembling a Rotating Disk Electrode (RDE) [4]. In this case, a rotating vacuum feed through is required. More recently, a wall-jet configuration was suggested [5] which led to defined convection at the electrode but quantitative kinetic measurements were not possible due to flow and mass transfer limitations.

Baltruschat and coworkers developed a thin-layer cell [6,7] for the use of massive electrodes under electrolyte flow. In such cells, the porous PTFE membrane is separated from the bulk electrode by a thin layer of electrolyte through which reaction products have to diffuse before they can be detected. Later on, dual thin layer cells [8–11] were developed which contain two liquid compartments: one reaction compartment and one detection compartment. Through this separation the reaction cannot be influenced by concentration changes because of transport of

* Corresponding author.
E-mail addresses: f.kubannek@tu-braunschweig.de (F. Kubannek), u.krewer@tu-braunschweig.de (U. Krewer).

Nomenclature

A_{el}	electrode area (m^2)
D	diffusion coefficient (m^2/s)
C_{dl}	capacity of the double layer (F)
E	electrode potential corrected for Ohmic drop vs. SHE (V)
E_{dl}	potential over the double layer (V)
$E_{external}$	uncorrected electrode potential vs. SHE (V)
F	Faraday constant (= 96485 C/mol)
I	total current (A)
$I_{reaction}$	current from electrochemical reactions (A)
I_{MS}	ion current (A)
K	DEMS calibration constant (C/mol)
K^*	MS calibration constant (C/mol)
N	collection efficiency of the DEMS cell
N_A	Avogadro constant (=6.022·10^13 1/mol)
$N_{surface}$	number of surface sites available for adsorption
Q_{dl}	charge in the double layer (C)
Q_m	charge for one monolayer of monovalent adsorbate (C)
R_{in}	cell radius at the inlet (m)
R_u	uncompensated electrolyte resistance (Ω)
R_{el}	electrode radius / cell radius at the bottom (m)
R	universal gas constant (=8.314 J/mol/K)
Re	Reynolds number (= vd/ν)
Sc	Schmidt number (= ν/D)
Sh	Sherwood number (= kR_{el}/D)
T	temperature (K)
$\dot{V}$	volume flow rate (m^3/s)
c	concentration (mol/m^3)
c_∞	bulk concentration (mol/m^3)
d_{in}	diameter of the inlet tube (m)
$g_{OH/CO}$	interaction factor for OH/CO
i_{lim}	limiting current density (A/m^2)
k	reaction rate constant (1/s)
$k_{CO,ad}$	adsorption rate constant for reaction II (1/s)
$k_{CO,ox}$	oxidation rate constant for reaction III (1/s)
$k_{OH,ad}$	adsorption rate constant for reaction I (1/s)
$k_{OH,de}$	desorption rate constant for reaction I (1/s)
$\dot{n}_{vac,CO_2}$	flow of CO_2 into the vacuum (mol/s)
$\dot{n}_{vac,CO}$	flow of CO into the vacuum (mol/s)
r	reaction rate ($mol/m^3/s$)
$r_{CO,ad/ox}$	adsorption / oxidation rate of CO (1/s)
$r_{OH,ad/de}$	adsorption / desorption rate of OH (1/s)
t_-	anion transference number
v_ϕ	tangential velocity at the electrode radius (m/s)
z	number of transferred electrons / coordinate perpendicular to the electrode surface (m)
$\alpha_{OH/CO}$	charge transfer coefficient for reaction I/III
$\beta_{OH/CO}$	symmetry factor for reaction I/III
δ	concentration boundary layer thickness (m)
δ_{el}	electrode thickness (m)
δ_{mem}	membrane thickness (m)
ϵ_{cat}	porosity of the electrode
ϵ_{mem}	porosity of the membrane
Θ_{CO}	relative surface coverage of CO
Θ_{OH}	relative surface coverage of OH
ν	kinematic viscosity (m^2/s)
ω	angular velocity (1/s)

reactants through the PTFE-membrane into the vacuum. The drawback of the thin-layer and double-thin layer cell is, however, the increased response time of about 1-2 seconds which results from the additional transport step from the electrode through the electrolyte to the PTFE-membrane. DEMS has also been combined with other analytical techniques such as EQCM [8] or FTIRS [12]. A double-band-electrode channel cell was presented by Abruña and coworkers [13] which featured a detection electrode for detecting non-volatile species. Also a number of cells featuring small pinhole or capillary inlets into the vacuum have been designed for the purpose of examining single crystal electrodes [14,7,15] or for scanning DEMS measurements [16].

A better understanding of processes in porous technical electrodes has a high practical and economic relevance. It is widely acknowledged that smooth model electrodes and porous electrodes differ in their electrochemical properties. Nevertheless there are only few works in which DEMS is utilized for analyzing technical electrodes: Pérez-Rodríguez et al. [17] examined high surface area electrocatalyst on a gas diffusion layer to analyze the effect of a microporous diffusion layer on transport using a classical DEMS cell with no convection. The same cell was also used to examine the effect of surface modifications on metallic mesoporous catalysts [18]. Niether and coworkers examined the oxidation of different fuels at high temperatures by DEMS using gas diffusion electrodes of high temperature PEMFCs [19]. Seiler et al. examined the kinetics of methanol and CO adsorption by DEMS using a fuel cell flow field as an electrode and a separate detection compartment at the outlet of the flow field [20]. However, the response times of these setups are quite high which is disadvantageous for analyzing dynamic processes and especially kinetics.

Nevertheless, the fast response times that could be attained by the classical DEMS cells make DEMS an attractive tool for analyzing micro- and macrokinetics of electrochemical reactions quantitatively. Early work on dynamic processes by Heitbaum and coworkers [21] has already demonstrated the feasibility of dynamic analysis by DEMS for the oxidation of formic acid on Platinum. Furthermore it has been shown before that dynamic modeling of reaction kinetics can yield new insights into the behavior of reaction systems, for example in case of the oxidation of methane in a catalytic monolith, i.e. a non-electrochemical reactor [22]. Zhang and coworkers [23] proposed a model for a DEMS thin-layer flow cell which was used for parametrizing a model for CO bulk oxidation on a smooth platinum electrode. In their publication no DEMS data was incorporated into the modeling, though.

To our knowledge, DEMS has not been used for identifying and parameterizing macro kinetic models of electrochemical reactions. In this article we will introduce a method for quantitatively determining rate constants for reactions on porous electrodes from dynamic DEMS measurements.

As mentioned above DEMS cells should be tailored to the experimental study. The main requirements for the goal stated above are as follows. When analyzing kinetics and formulating rate expressions of electrochemical reactions, the rate determining step can depend on the concentration of reactants. This is the case for example if an adsorption step following the Langmuir, Frumkin or Temkin adsorption is rate determining. Furthermore, there is evidence that for example the proportion of completely oxidized products of the methanol oxidation reaction on certain catalysts is influenced by desorption and readsorption of intermediates [24]. Clearly, a good understanding of the concentration distribution at the surface is important to distinguish the influence of diffusion limitations and reaction limitations. Thus a defined - preferably homogeneous - concentration boundary layer is the first requirement for our cell. For many of the existing DEMS cells the concentration profile at the electrode surface is not very reproducible or quite inhomogeneous [25,14]. The second important

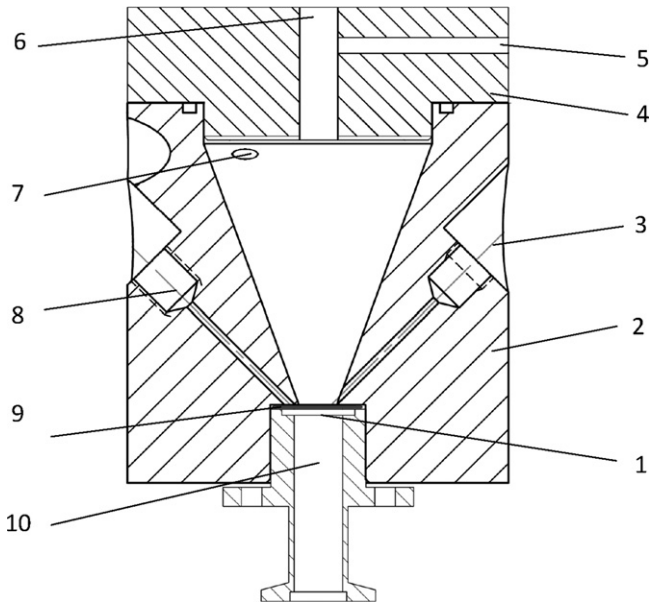

Fig. 1. Design of the cyclone flow DEMS cell, including: (1) stainless steel frit,(2) cell body from Kel-F, (3) connection to reference electrode, (4) cell cap from Kel-F, (5) electrolyte outlet, (6) connection to counter electrode, (7) tangential electrolyte inlet, (8) Pt-wire as current collector, (9) working electrode on porous PTFE membrane and gasket, (10) connection to vacuum system / MS

requirement is a short response time of the MS signal. It is essential for analyzing fast reaction steps and applying high scan rates.

In the present work we will first introduce a new DEMS cyclone flow cell for analyzing kinetics of technical electrodes quantitatively. Next we will analyze the flow behavior and especially the concentration boundary layer by CFD simulations and experiments. Furthermore we will evaluate calibration measurements for CO_2. Results of the CFD simulations and the calibration measurements will be utilized for setting up a physical model that quantitatively describes the oxidation of CO on a carbon supported Pt/Ru catalyst. The kinetic parameters will be identified using experimental data obtained with the DEMS cyclone flow cell.

2. Experimental

2.1. Cell design

The design of the cyclone flow DEMS cell is depicted in Fig. 1. The solution enters the cell through a 2 mm diameter hole tangential to the cell wall (7), moves downwards along the cell walls in a vortex flow circulating over the working electrode (9) at the bottom of the cell, and rises up again in the middle of the cell. A detailed analysis of the flow is presented in section 4.1. The fluid leaves the cell through the outlet on top (5). The counter electrode (6) is placed downstream of the working electrode to prevent reaction products from counter electrode to reach the working electrode. The working electrode is deposited directly onto a porous PTFE membrane at the bottom of the cell through which volatile species can enter the vacuum system. This leads to a minimal response time because the transport path of species produced at the electrode is short. The membrane is supported by a stainless steel frit (1) to withstand the pressure difference between the liquid compartment and the vacuum system beneath (10). Closely above the membrane a Luggin capillary leading to the reference electrode (3) is placed. The cell body is made from PCTFE (Kel-F), seals are made from Viton. The upper cell radius is 60 mm, the angle of the cone walls is 40 degrees, and the lower cell radius is 0.5 cm resulting in an electrode area A_{el} of 0.785 cm^2.

2.2. Residence time measurements

As part of the flow analysis, residence time distributions were recorded: deionized water was pumped from a reservoir through the cyclone cell and the conductivity of the solution at the outlet was monitored continuously by a conductivity meter (S230, Mettler Toledo). Then a three-port-valve was switched rapidly to change to a different reservoir and hydrochloric acid solution was pumped through the cell. The experiment was stopped when the conductivity at the outlet reached that of the hydrochloric solution. Finally, the curves were normalized and corrected for the delay caused by the tubing between the reservoir and the cell.

2.3. DEMS setup

The setup consists of two vacuum chambers separated by an adjustable valve. The first chamber, which is connected to the cyclone flow cell, is evacuated by a turbo-molecular pump (HiPace300, 260 L/s, Pfeiffer Vacuum) backed by a membrane vacuum pump (MVP 015-4, Pfeiffer Vacuum). The second chamber which contains the mass spectrometer (Pfeiffer QMG220 M1 quadropole mass spectrometer with secondary ion multiplier) is evacuated by a second turbo-molecular pump (HiPace 80, 67 L/s, Pfeiffer Vacuum) backed by a rotary vane pump (Duo 5M, Pfeiffer Vacuum). The pressure in both compartments is monitored by two vacuum pressure sensors. A Gamry Reference 3000 potentiostat is used for the electrochemical experiments. A LABVIEW program specially developed for this purpose is used to record MS and potentiostat data. Ten data points are collected per second to reduce the noise in the MS signal.

2.4. Solutions and electrode preparation

Solutions were prepared with ultrapure water (Millipore Milli-Q 18.2 MΩcm). 0.25 M Perchloric acid (Sigma Aldrich, ACS grade) was used as a supporting electrolyte for electrochemical measurements. CO-saturated solutions were prepared by bubbling CO (99.97 %, Westfalen AG) for at least 20 minutes through the electrolyte. To produce the porous electrodes, the catalyst Pt/Ru (1:1) on 40% w/w carbon black (Johnson Matthey, HiSpec 10000) was mixed with ultrapure water, Isopropanol (VWR, HPLC grade), and Nafion solution (5% w/w of catalyst weight, Qintech NS05), ultrasonicated for 20 minutes in ice water and then spray coated with a stream of Nitrogen (99.999% Westfalen AG) directly onto the PTFE-membrane (Pall Membranes, specified pore size 0.2 μm). To determine the thickness and porosity of the Pt/Ru catalyst layer, the cross section of a membrane with catalyst layer of the same type was examined by SEM. The thickness of the membrane is approximately $\delta_{mem} = 60\,\mu m$ and the thickness of the catalyst layer is approximately $\delta_{el} = 25\,\mu m$. From the catalyst loading and the densities of platinum (21.5 g/cm^3), ruthenium (12.5 g/cm^3), carbon black (2 g/cm^3) and Nafion (1.8 g/cm^3), a porosity of $\epsilon_{cat} = 0.92$ is calculated according to equations (1) and (2).

$$\epsilon_{cat} = 1 - \frac{V_{solid}}{V_{electrode}} \tag{1}$$

$$V_{solid} = \frac{m_{catalyst}}{\rho_{catalyst}} + \frac{m_{carbon}}{\rho_{carbon}} + \frac{m_{nafion}}{\rho_{nafion}} \tag{2}$$

In the literature porosities of 80% ±5% have been reported for catalyst layers in hot-pressed MEAs when there was no carbon in the catalyst. Thus, the porosity lies within a reasonable range. In the same way the porosity of the expanded PTFE membrane is calculated from the thickness and weight of the membrane and the density of non-porous PTFE (2.2 g/cm^3) as $\epsilon_{mem} = 0.72$.

The counter electrode was made from a platinum wire. Measurements were conducted at room temperature of $25 \pm 0.5\,^{\circ}C$. A commercial saturated Silver/ Silver-Chloride electrode (Meinsberg-Elektroden) was used as reference electrode. All potentials are, however, reported with respect to the potential of a reversible hydrogen electrode.

For the MS calibration, CO_2 (99.999 %, Westfalen AG) was leaked into the first vacuum chamber through an adjustable leak valve.

3. Modeling

3.1. Computational fluid dynamics

The computational fluid dynamics (CFD) simulations of the cyclone flow cell are carried out using the commercial finite volume code FLUENT 15.07. A pressure-based solver was selected because of the incompressible nature of the flow. The partial differential equations were discretized using the SIMPLEC (Semi-Implicit Method for Pressure-Linked Equations-Consistent) method for pressure - velocity coupling and the Second Order Upwind scheme for pressure and momentum interpolation. The SST k-ω turbulence model was chosen because of the rather low Reynolds numbers near the bottom of the cyclone cell. It should be noted that the Reynolds numbers of the flow in gas cyclones for the separation of particles are usually higher so that different turbulence models are preferred for such flows [26]. A mesh independency study was performed and a 900,000 element unstructured mesh of tetraeders including inflation layers at the walls was used for the simulations. Boundary conditions are constant velocity at the inlet, constant pressure at the outlet and no-slip at the walls. For the flow simulation, the Luggin capillary is not taken into account.

Also transient calculations were performed to validate the CFD results by comparing them to experimental residence time distributions. After the fluid flow was fully developed, the boundary condition at the inlet was changed and a second species was introduced. Monitoring the concentration of the second species at the outlet over time yields the residence time distribution.

When analyzing reaction kinetics, the concentration boundary layer in the diffusion limited case is of primary interest. The diffusion limited conditions are modeled by introducing a species A (5% w/w, $D = 2.03 \cdot 10^{-9}\,m^2/s$ based on dissolved carbon monoxide. 5% w/w exceeds the solubility of carbon monoxide at ambient pressure; we use such a high value to avoid numerical errors) at the inlet that reacts at the bottom of the cell to a species B with the same density and diffusion properties. The rate constant of the surface reaction is set very large (10^{15}) so that the concentration of species A at the surface approaches zero. This scenario allows to use Fluent's built in reaction module and is similar to a diffusion limited electrochemical reaction since the conversion rate only depends on the mass transfer towards the surface. Diffusion limited reaction rates - i.e. mass transfer rates - are calculated from the amount of species A converted to B and can easily be expressed in terms of a limiting current density.

3.2. Model for CO oxidation at a porous electrode

In this section we set up a dynamic model of the porous Pt/Ru electrode described in section 2.4. The outputs - current and the amount of CO_2 entering the DEMS vacuum system - can be directly compared to experimental data which we obtain for CO bulk oxidation. By matching experimental and simulated data, rate constants are determined.

CO oxidation on Pt/Ru follows a two step mechanism consisting of the dissociative adsorption of water and the reaction of adsorbed OH and adsorbed CO to CO_2. The first of these steps is reversible.

$$H_2O \underset{r_{OH,de}}{\overset{r_{OH,ad}}{\rightleftharpoons}} OH_{ad} + H^+ + e^- \quad \text{(I)}$$

$$CO \overset{r_{CO,ad}}{\longrightarrow} CO_{ad} \quad \text{(II)}$$

$$CO_{ad} + OH_{ad} \overset{r_{CO,ox}}{\longrightarrow} CO_2 + H^+ + e^- \quad \text{(III)}$$

We model the CO oxidation kinetics on Pt/Ru similarly to [31] where the oxidation of pre-adsorbed CO on a Pt/Ru catalyst without carbon is examined in an RDE setup. The relative surface coverages of OH and CO change over time by adsorption, desorption and oxidation:

$$\frac{d\,\Theta_{OH}}{d\,t} = r_{OH,ad} - r_{OH,de} - r_{CO,ox} \quad (3)$$

$$\frac{d\,\Theta_{CO}}{d\,t} = r_{CO,ad} - r_{CO,ox} \quad (4)$$

Θ_{OH} and Θ_{CO} denote the relative surface coverages of OH and CO, $r_{OH,ad}$ and $r_{OH,de}$ are the OH adsorption and desorption rates respectively (reaction (I)). $r_{CO,ad}$ is the CO adsorption rate (reaction (II)) and $r_{CO,ox}$ is the final oxidation step (reaction (III)).

The Frumkin/Temkin adsorption isotherm is assumed for OH [31], Langmuir adsorption for CO [32]. Significant exchange rates between dissolved and adsorbed CO were found in a study by Heinen et al. [27]. This process is not taken into account here because in the chosen mean field approximation with area-averaged values of the relative coverage, the overall oxidation rate is not influenced by such an exchange step. Other experimental studies [28,29] show that CO desorption which would yield free adsorption sites can be neglected for experiments lasting only several minutes. The adsorption and reaction rates are thus described by equations (5) to (8).

$$r_{OH,ad} = k_{OH,ad}(\Theta) \cdot (1 - \Theta_{OH} - \Theta_{CO}) \cdot \exp\left(-\frac{(1-\alpha_{OH}) \cdot F \cdot E}{R \cdot T}\right) \quad (5)$$

$$r_{OH,de} = k_{OH,de}(\Theta) \cdot \Theta_{OH} \cdot \exp\left(\frac{\alpha_{OH} \cdot F \cdot E}{R \cdot T}\right) \quad (6)$$

$$r_{CO,ox} = k_{CO,ox}(\Theta) \cdot \Theta_{OH} \cdot \Theta_{CO} \cdot \exp\left(\frac{\alpha_{CO} \cdot F \cdot E}{R \cdot T}\right) \quad (7)$$

$$r_{CO,ad} = k_{CO,ad}(\Theta) \cdot (1 - \Theta_{OH} - \Theta_{CO}) \cdot c_{CO} \quad (8)$$

Water concentration is assumed not to change during the reaction and thus included into the rate constant because there is a great excess of water. For Frumkin/Temkin adsorption conditions, the rate constants depend on the relative surface coverages and the interaction / symmetry factors g and β:

$$k_{OH,ad} = k_{0,OH,ad} \cdot \exp(\beta_{OH} g_{OH} \Theta_{OH}) \quad (9)$$

$$k_{OH,de} = k_{0,OH,de} \cdot \exp((1 - \beta_{OH}) g_{OH} \Theta_{OH}) \quad (10)$$

$$k_{CO,ox} = k_{0,CO,ox} \cdot \exp(\beta_{CO} g_{CO} \Theta_{CO} + \beta_{OH} g_{OH} \Theta_{OH}) \quad (11)$$

It has already been pointed out that mass transfer inside porous electrodes plays an important role in a DEMS setup where the electrode is directly deposited on the PTFE membrane [30,4]. Considering the results of the CFD simulations which will be discussed in section 4.1, we only take into account transport processes and gradients in the direction perpendicular to the electrode. We assume that transport inside the boundary layer and the porous media is of purely diffusive nature. Thus the local concentrations

of CO (c_{CO}) and CO_2 (c_{CO_2}) in the electrolyte boundary layer are described by the following partial differential equations:

$$\frac{\partial c_{CO}}{\partial t} = D_{CO,electrolyte}\frac{\partial^2 c_{CO}}{\partial z^2} \tag{12}$$

$$\frac{\partial c_{CO_2}}{\partial t} = D_{CO_2,electrolyte}\frac{\partial^2 c_{CO_2}}{\partial z^2} \tag{13}$$

In the catalyst layer the porosity and the reaction are taken into account:

$$\frac{\partial c_{CO}}{\partial t}\cdot\epsilon_{cat} = D^{eff}_{CO,cat}\frac{\partial^2 c_{CO}}{\partial z^2} - \frac{r_{CO,ad}}{A_{el}\cdot\delta_{el}}\cdot\frac{N_{surface}}{N_A} \tag{14}$$

$$\frac{\partial c_{CO_2}}{\partial t}\cdot\epsilon_{cat} = D^{eff}_{CO_2,cat}\frac{\partial^2 c_{CO_2}}{\partial z^2} + \frac{r_{CO,ox}}{A_{el}\cdot\delta_{el}}\cdot\frac{N_{surface}}{N_A} \tag{15}$$

The transport through the porous membrane is described by equations (16) and (17):

$$\frac{\partial c_{CO}}{\partial t}\cdot\epsilon_{mem} = D^{eff}_{CO,mem}\frac{\partial^2 c_{CO}}{\partial z^2} \tag{16}$$

$$\frac{\partial c_{CO_2}}{\partial t}\cdot\epsilon_{mem} = D^{eff}_{CO_2,mem}\frac{\partial^2 c_{CO_2}}{\partial z^2} \tag{17}$$

$D_{i,j}$ is the diffusion coefficient of species i, i.e. CO or CO_2 in j $\in$ {electrolyte, electrode, membrane}; z is the coordinate perpendicular to the electrode. $N_{surface}$ is the total number of available surface sites and A_{el} is the electrode area. As above, it is assumed that the water concentration does not change significantly through the reaction. Thus, water transport is not modeled.

The diffusion coefficients of CO and CO_2 in the electrolyte are assumed to be equal to those in water: $D_{CO,H_2O} = 2.03\cdot10^{-9}$ m/s^2 at 25 °C [33], $D_{CO_2,H_2O} = 1.92\cdot10^{-9}$ m/s^2 at 25 °C [33]. The effective diffusion coefficients in the porous electrode and membrane are assumed to follow the Bruggeman equation:

$$D^{eff}_{i,j} = D_{i,H_2O}\cdot\epsilon_j^{1.5} \tag{18}$$

With porosities ϵ_j being that of the electrode or membrane. The thicknesses of membrane and electrode were determined by SEM as described above, whereas the thickness of the concentration boundary layer is determined from CFD simulations.

As boundary conditions, the concentrations of all species are fixed to zero at the membrane/vacuum interface and to their bulk values at the outer edge of the concentration boundary layer:

$$c_{CO}|_{z=0} = c_{CO,bulk} \tag{19}$$

$$c_{CO2}|_{z=0} = c_{CO2,bulk} \tag{20}$$

According to the experimental conditions (compare section 2), the CO bulk concentration is set to saturation concentration (1.1 mol/m^3 at 20 °C) whereas the CO_2 bulk concentration is set zero.

At the membrane/vacuum interface all concentrations are fixed to zero. The initial values of all concentrations and surface coverages were equal to the steady state values at a fixed potential in our simulations. The steady state values were found by simulating the model for a long time starting from arbitrary initial values.

The double layer is modeled as a capacitor with constant capacitance C_{dl} according to [34]. The charge stored in the double layer is the integral of the total current minus the Faradaic currents from reactions (I) and (III):

$$\frac{dQ_{dl}}{dt} = \frac{dE}{dt}\cdot C_{dl} = I - I_{reaction} \tag{21}$$

$$I_{reaction} = Q_m\cdot(r_{CO,ox} + r_{OH,ad} - r_{OH,de}) \tag{22}$$

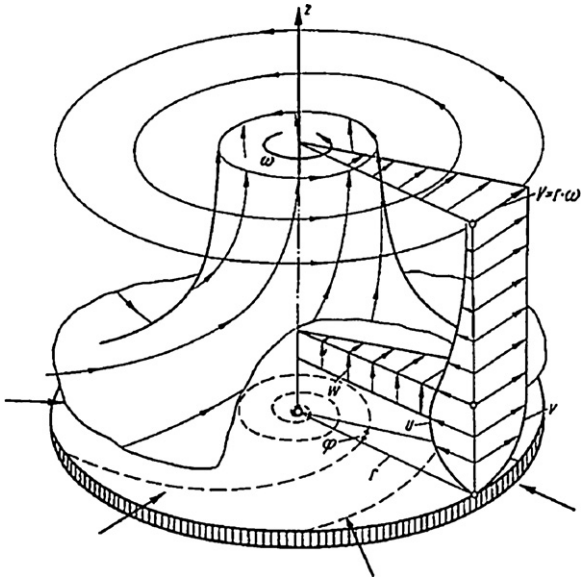

Fig. 2. Ideal vortex flow field [35], with courtesy of Springer

With $Q_m = F\cdot N_{surface}/N_A$ being the charge of one monolayer of adsorbed molecules on the catalyst surface.

The apparent potential between the working electrode and the reference electrode $E_{external}$, which can be measured in an experiment by a potentiostat, is slightly larger due to the uncompensated solution resistance R_u:

$$E_{external} = E + R_u I \tag{23}$$

The amount of CO_2 and CO entering the vacuum system is calculated from the concentration gradient at the membrane/vacuum interface according to equations (24) and (25) where A_{el} denotes the electrode area.

$$\dot{n}_{vac,CO_2} = -D^{eff}_{CO_2,mem}\cdot A_{el}\cdot\left(\frac{\partial c_{CO_2}}{\partial z}\right)\Big|_{mem/vac} \tag{24}$$

$$\dot{n}_{vac,CO} = -D^{eff}_{CO,mem}\cdot A_{el}\cdot\left(\frac{\partial c_{CO}}{\partial z}\right)\Big|_{mem/vac} \tag{25}$$

We assume that transport inside the vacuum system is fast and that there is no holdup [30].

To solve this set of equations, the concentration boundary layer inside the electrolyte from section 4.1, the electrode, and the membrane are discretized in z-direction, perpendicular to the electrode surface, with the finite volume method assuming piecewise linear profiles. Each layer is discretized into 40 elements and the resulting ordinary differential equations are solved numerically by Matlab solver ode23t.

The values of geometric parameters used for the simulation are the same as in the experimental setup. The values and identification procedure for the kinetic parameters are discussed in the results section 4.3.

4. Results and discussion

4.1. Flow analysis of the cyclone cell

Sundmacher [35] proposed a cyclone flow cell for investigating gas diffusion electrodes under defined mass transfer conditions. In such a cell, a vortex flow field is established where the fluid is circulating above a stationary electrode. In Fig. 2 the flow pattern of an ideal vortex is depicted. The fluid rotates inwards above an infinite stationary plane at a constant angular velocity ω. In the

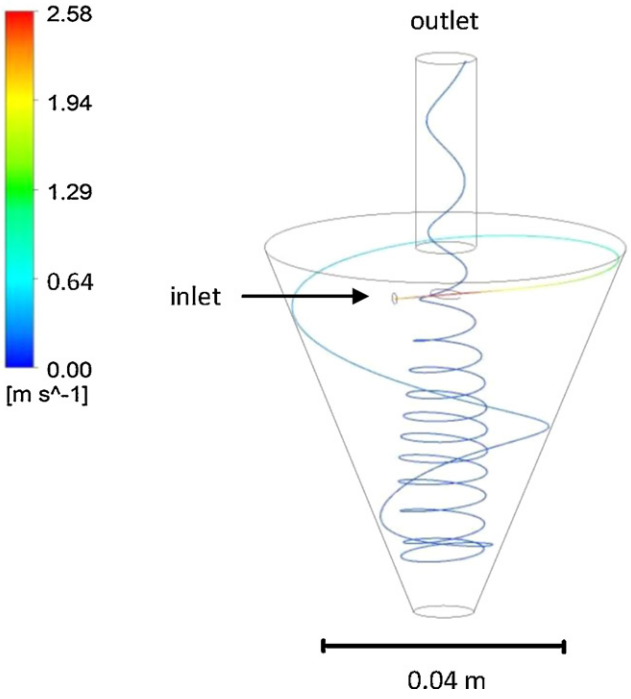

Fig. 3. Simulated pathline and velocity of a single particle introduced at the inlet of the cyclone for a flow rate of 216 ml/min

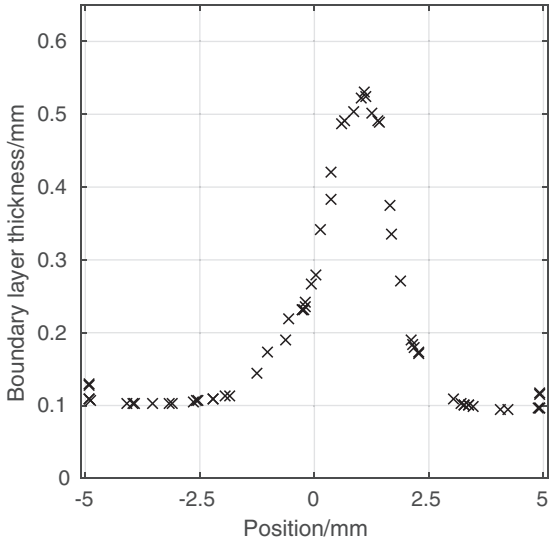

Fig. 4. Simulated concentration boundary layer thickness as function of the distance from the electrode center at a flow rate of 216 ml/min

center of the vortex the fluid rises upwards. This flow regimen is very promising because it has been shown that an ideal vortex flow yields a constant hydrodynamic boundary layer thickness δ_V for a given rotation speed which is twice as thick as that of an RDE at the same rotation speed [36,37]:

$$\delta_V = 8\left(\frac{\nu}{\omega}\right)^{1/2} \tag{26}$$

There are also other flow patterns which result in well-defined mass transfer to an electrode [38]. The RDE, the wall-tube, and wall-jet electrode yield well-defined and in case of the former two also homogeneous mass transfer. A wall-jet flow cell has been used successfully for studying CO oxidation kinetics [39,40]. The cyclone flow cell employed in this study is comparatively easy to produce for DEMS experiments because there are no moving parts and the membrane can be sealed easily.

However, since the surface area in a cyclone cell is not infinite, cyclone walls are expected to have a significant influence on the flow. Sundmacher [35] analyzed the cyclone flow in theory without taking into account wall friction and without analyzing the thickness of the concentration boundary layer in detail. As discussed in the introduction, such information is important for analyzing kinetics of porous electrodes quantitatively. To get a deeper insight into the flow pattern and especially the shape of the boundary layer, numerical flow simulations (CFD) are performed.

In Fig. 3, the pathline of a single particle through the cell is illustrated. As expected, the fluid flows along the outer walls towards the bottom of the cell rising up in the center, producing a vortex above the membrane. There are some deviations from the ideal flow though: In an ideal vortex flow field the flow is axisymmetrical. The center of the cyclone flow does, however, not exactly correspond to the geometrical center of the cell which we ascribe to the positioning of the inlet. Classical cyclones for the separation of particles from a gas stream also show such a non-symmetric flow pattern [26]. Furthermore, for ideal vortex flow, the tangential velocity at the inner radius is not a function of the distance from the electrode. While the CFD results do not show a dependency of the tangential velocity on the distance from the electrode either (only in a small part of the cyclone near the inlet), the magnitudes of the tangential velocities from the CFD simulations are lower by a factor of 20 (100 ml/min) to 60 (590 ml/min) compared to the theoretical calculations in [35]. We attribute this to wall friction and fluid-fluid interaction between the flow in the center and the fluid descending along the outer walls which was not taken into account in the cited reference.

To obtain information about the concentration boundary layer under diffusion limited conditions, a surface reaction is introduced as explained in section 3.1. In Fig. 4, the thickness of the resulting concentration boundary layer, defined by $c_{boundary} = 0.9c_\infty$, for a flow rate of 590 ml/min for a mass transfer limited surface reaction is plotted over the electrode radius. It can be seen that the boundary layer has a relatively constant thickness between $R = 2.5 \cdot 10^{-3}$ m and $R = 5 \cdot 10^{-3}$ m. In the center where the fluid rises up, the boundary layer is much thicker. Thus only the outer part of the electrode features a homogeneous boundary layer. It should be noted, however, that this segment represents 75% of the total electrode area. The inner 25 % of the electrode area feature a much thicker and less homogeneous boundary layer.

According to theory, the boundary layer thickness of a vortex flow should be proportional to angular velocity ω to the power of -0.5 (compare equation (26)). Sundmacher predicts a linear relationship between angular velocity and the inlet velocity which is directly correlated to the volume flow $\dot{V}$ via the inlet tube diameter d_{in} and the radius of the cyclone flow cell at the height of the inlet tube R_{in} [35]:

$$\omega = \frac{v_\phi}{R_{el}} = v_{inlet} \cdot \sqrt{\frac{R_{in}}{R_{el}}} \cdot \frac{1}{R_{el}} = \frac{4\dot{V}}{\pi d_{in}^2} \cdot \sqrt{\frac{R_{in}}{R_{el}}} \cdot \frac{1}{R_{el}} \tag{27}$$

Thus, it would be expected that since δ is proportional to $\omega^{-1/2}$ it would also be proportional to $\dot{V}^{-1/2}$. In Fig. 5, the thickness of the homogeneous part of the boundary layer ($R > 0.5R_{el}$) over the flow rate is depicted. Contrary to the prediction, a relationship of $\delta \propto \dot{V}^{-0.8}$ is obtained as the best fit. To rationalize this result, the dependency of angular velocity obtained from the simulation against flow rate is analyzed. Angular velocity changes with the r and z-coordinate only very near the inlet tube, as explained above. Thus a direct correlation between flow rate and angular velocity can be obtained. It is found not not to be directly proportional to

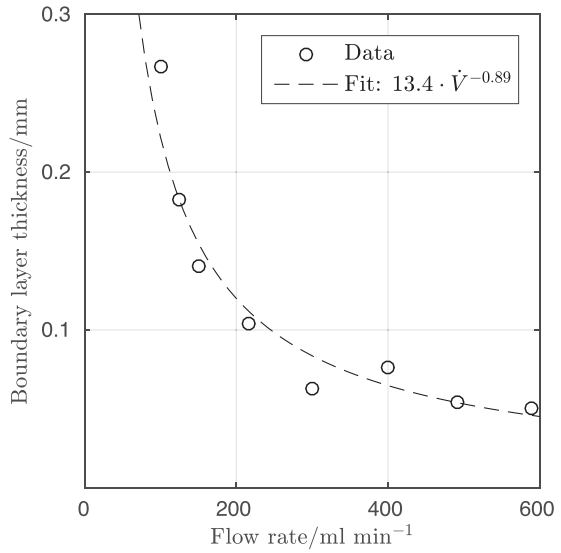

Fig. 5. Simulated concentration boundary layer thickness for $R > 0.5R_{el}$ and different flow rates

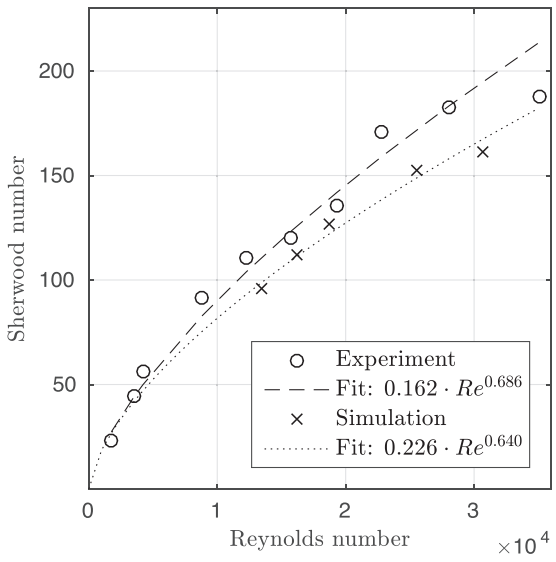

Fig. 6. Sherwood number over Reynolds number from experiment and simulation, $\nu_{mixture} = \nu_{H_2O} = 1.0410^{-6}$ m^2/s, $D_{A/B} = 0.8410^{-9}$ m/s [33], $D_{CO_2/H_2O} = 1.9210^{-9}$m/s [33], solubility of CO_2 in water: 1.5 g/kg (23 °C) [41]

volume flow but to volume flow to the power of 1.68 (see Fig. 12 in the appendix). Combining these two findings we obtain:

$$\omega \propto \dot{V}^{1.68} \rightarrow \dot{V} \propto \omega^{1/1.68} \tag{28}$$

$$\delta \propto \dot{V}^{-0.89} \rightarrow \delta \propto \omega^{-0.89/1.68} = \omega^{-0.52} \tag{29}$$

Thus the relationship $\delta \propto \omega^{1/2}$ is confirmed by the CFD simulation results whereas the dependence of ω on $\dot{V}$ seems to follow a different relation than predicted before - which is also supported by the deviation of the tangential velocity from the value calculated by Sundmacher [35] by an order of magnitude. For small cyclone flow cells, therefore, further studies should be conducted and the model by Sundmacher would need to be extended to cover non-ideal behavior.

To validate the CFD calculations, residence time distributions were determined experimentally and simulated in Fluent; the experimental residence time distributions are reproduced well by the simulations (see Fig. 13 in the appendix). Furthermore, variation of the diffusion coefficient in the simulation (see Fig. 14 in the appendix) leads to the well known behavior of $r_{lim} \propto D^{2/3}$ resulting from laminar boundary theory [35,25].

In DEMS experiments there is a further transport resistance because volatile species have to pass the porous PTFE membrane before entering the vacuum system. Therefore it is important to check if the transport of volatile species through the membrane into the vacuum is still proportional to the flow rate to the power of two-thirds. Here, mass transfer relations will be obtained from the flow analysis and expressed in terms of dimensionless numbers. Based on these numbers, we will compare our CFD results with those from literature and experiments including the transport through the membrane. For this purpose, a solution saturated with CO_2 was pumped through the cell at different flow rates and the ion current was recorded by the mass spectrometer. The amount of CO_2 entering the vacuum can be determined using the calibration constant K^* of the MS which will be discussed in the next section.

Sundmacher defined the Reynolds number for the cyclone flow cell as a function of electrode radius R_{el}, cyclone radius at inlet height R_{in}, diameter of the tangential inlet d_{in}, volume flow, and viscosity:

$$Re = \frac{4\dot{V}}{\pi d_{in}^2} \frac{\sqrt{R_{in} R_{el}}}{\nu} \tag{30}$$

and experimentally obtained the following mass transfer relation in terms of dimensionless numbers for the cyclone flow cell:

$$Sh = \frac{q}{1 - t_-} Re^{2/3} Sc^{1/3} \quad (\text{for } Re > 10^3 \text{ and } Sc \geq 1) \tag{31}$$

Sh denotes the Sherwood number, *Sc* the Schmidt number, t_- the anion transference number, and $q = 0.0136$ is a constant. In Fig. 6, the Sherwood numbers from our experiment and simulation are depicted as a function of the Reynolds number as defined by equation (30). Mass transfer is proportional to flow rate to the power of two third in experiment and simulation, matching the relation obtained by Sundmacher. Thus the mass transfer to the vacuum in the DEMS cell can also be described by equation (31). Since the experimental data obtained by Sundmacher and in this work only covers Reynolds number between approximately 1000 and 35000, we recommend using the equations only with great care outside this region. From equation (31) a Levich-type equation for the DEMS cyclone flow cell can be derived. Although both formulations contain the same information, we include the Levich-type equation in the appendix because it might be more familiar to some readers. For the constant q we obtain 0.021 from the simulation and 0.023 from the experiment. Experiment and simulation are thus in good agreement. The values do, however, differ slightly from the one obtained by Sundmacher.

We believe that further investigation of the relationship between geometry parameters and the fluid velocity at the electrode and a review of the definition of the Reynolds number are necessary in order to be able to generalize equation (31) and the relation for the boundary layer thickness for cyclones of all kinds of shapes. Such an investigation might also resolve the difference in the constant q between our and the previous experimental results. For the purpose of conducting DEMS experiments under conditions of defined external mass transfer, the obtained relationship for the presented cell is sufficient, though.

4.2. DEMS calibration for CO_2

For quantitative analysis, calibration of the DEMS setup is necessary. Two separate calibration steps are performed: since not all molecules in the vacuum system get ionized and detected, the first calibration constant K^* describes the relationship between the

amount of substance entering the vacuum system $\dot{n}_{vacuum}$ and the ion current I_{MS} at a fixed value m/z [30,42,43]:

$$K^* = \frac{I_{MS}}{\dot{n}_{vacuum}} \tag{32}$$

Because not all volatile species $\dot{n}_{reaction}$ which are produced in a reaction at the electrode enter the vacuum system, a second calibration constant K is defined. Besides K^* it takes into account the collection efficiency $0 \leq N = \frac{\dot{n}_{vacuum}}{\dot{n}_{reaction}} \leq 1$ of the cyclone cell which is influenced not only by the vacuum system and the MS itself but also by properties of the electrode and the membrane:

$$K = N \cdot K^* = \frac{I_{MS}}{\dot{n}_{reaction}} \tag{33}$$

In order to determine K^*, the vacuum system is connected through a leak valve to a chamber of known volume that can be filled with calibration gas. When monitoring the amount of gas leaking into the vacuum system and the ion current simultaneously, K^* can be determined.

Former studies already concluded that the electrochemical cell should be connected during calibration [30] because water diffusing through the membrane changes the total pressure as well as the ionization probabilities and thus influences the calibration constants for other substances.

The pressure in the calibration volume is generally very low because the calibration should preferably be performed at conditions close to the operating conditions. The temperature does not change significantly during the experiment because the heat capacity of the metal walls enclosing the calibration volume is very large compared to that of the gas inside. Thus, the ideal gas law can be employed to calculate the amount of gas flowing into the vacuum system as a function of the pressure inside the calibration volume:

$$\dot{n}_{vacuum} = -\frac{dp}{dt}\frac{V}{RT} \tag{34}$$

$$K^* = \frac{I_{MS}}{\dot{n}_{vacuum}} = -I_{MS}\frac{RT}{V}\left(\frac{dp}{dt}\right)^{-1} \tag{35}$$

Fig. 8 shows the plot of ion current at m/z = 44 versus derivative of the pressure during calibration for CO_2. A linear correlation is observed and from the slope of the regression curve, K^* = 0.186 C/mol is calculated. Although it has been pointed out previously that the pressure measurement is a potential error source [42], this value was found to be very reproducible in our experiments with a standard deviation of 1.2% (n=3).

To obtain the DEMS calibration constant K for CO_2, we employ the CO oxidation reaction. Since CO_2 is the only reaction product, the amount of CO_2 produced at the electrode can be calculated from the Faradaic current I. K can be calculated from the following equation [30]:

$$K = N \cdot K^* = \frac{I_{MS}}{\dot{n}_{reaction}} = \frac{I_{MS} \cdot z \cdot F}{I} \tag{36}$$

where z = 2 is the number of electrons transferred per molecule of CO_2.

CO-stripping during a CV is often used for calibration [30]. Since double layer contributions to the Faradaic current can be large especially for technical electrodes with high surface areas [44], we use steady state measurements at a constant electrolyte flow rate of 430 ml/min for obtaining the calibration constant. For this purpose, the potential of the working electrode is stepped from a steady state at 0.45 V to 0.65 V and back again after reaching a second steady state. In Fig. 7, the Faradaic and ion currents during a positive and a negative step are shown. The higher and lower potential are chosen based on cyclic voltammograms so that the lower potential is just above the onset potential of CO oxidation on Pt/Ru catalysts and the higher potential is well above the peak potential [44]. The

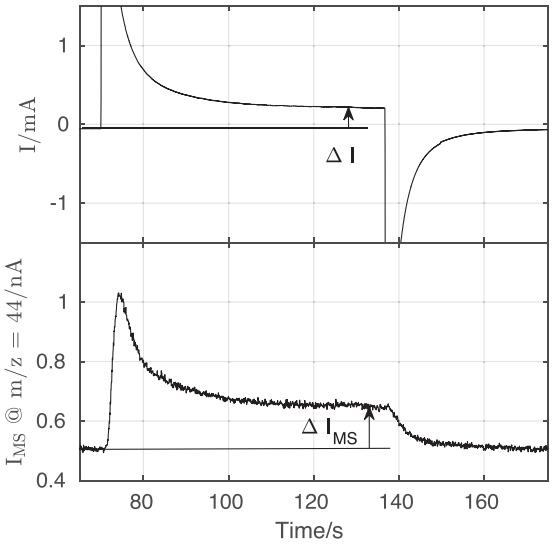

Fig. 7. Faradaic current I and ion current I_{MS} over time for CO bulk oxidation. The potential is stepped from 0.45 V to 0.65 V at t = 72s and back to 0.45 V at t = 137s at a flow rate of 430 ml/min for the CO-saturated electrolyte containing 0.25 mol/L $HClO_4$

steady state change in Faradaic current and ion current (ΔI_F and ΔI_{MS} in Fig. 7) is inserted into equation (36). This way, no additional background correction is required.

For CO_2 K = 0.115 C/mol is obtained. In four subsequent step experiments using the same electrode, we obtained a mean value of 0.117C/mol with a standard deviation of 6.7%. This corresponds to a collection efficiency of N = 62% for CO_2. The value of K is specific for the chosen electrode geometry, electrolyte flow rate and composition, and the vacuum system / MS device. It can be expected that the collection efficiency drops at higher electrolyte flow rates because a larger share of the volatile products will diffuse into the electrolyte when the thickness of the diffusion layer decreases. Tegtmeyer and coworkers [4] present a very clear explanation for this phenomenon. In the next section an estimation of the collection efficiency of the cyclone cell will be discussed.

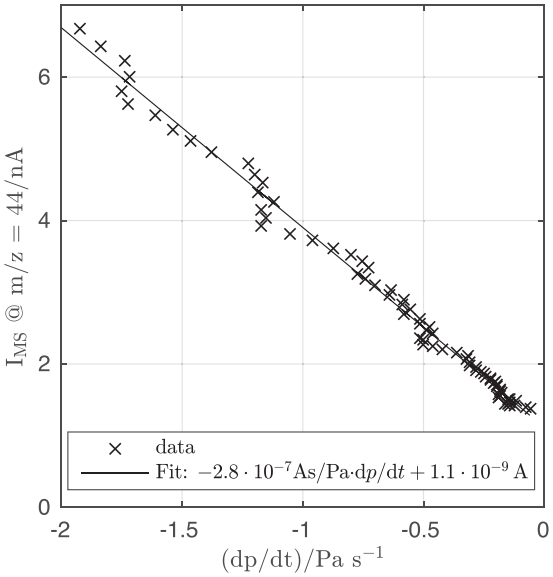

Fig. 8. Ion current at m/z = 44 over the derivative of the pressure in the calibration volume while CO_2 is leaked into the vacuum system

Table 1
Kinetic parameters for the CO oxidation modeling

parameter	Value	Unit	
$k_{0,OH,ad}$	$0.0026 \cdot 10^{-5}$	s^{-1}	fitted
$k_{0,OH,de}$	$2.17 \cdot 10^{11}$	s^{-1}	fitted
$k_{0,CO,ox}$	$2.01 \cdot 10^{-6}$	s^{-1}	fitted
$k_{CO,ad}$	0.305	s^{-1}	fitted
$N_{surface}$	$4.09 \cdot 10^{16}$	-	fitted
g_{CO}	27.3	-	fitted
g_{OH}	13	-	[44]
α_{OH}	0.5	-	[44]
α_{CO}	0.5	-	[44]
β_{OH}	0.5	-	[44]
R	29.8	Ω	fitted
C_{dl}	0.0776	F	fitted

Obviously, this relation does not hold right after the potential step. The dynamic behavior will be discussed more detailed in section 4.3. In the same experiment, a calibration constant for CO can be obtained by monitoring the decrease of the CO signal instead of the increase of the CO_2 signal (not shown here). The CO signal at m/z = 28 contains a comparatively large background signal from nitrogen. Moreover, CO_2 produces a signal at m/z = 28, too. The fact that different ions may contribute to the signal at a given m/z ratio has been discussed in literature before [45,3,46]. We found that the intensity of the CO_2 signal at m/z = 28 was 18.4 % of the intensity at m/z = 44 in our setup. In literature, a value of 12.6 % was reported for experiments conducted with a slightly higher ionization energy [47]. After applying a correction for the contribution of CO_2 to the signal at m/z = 28, a calibration constant of $K = 0.09$C/mol is obtained for CO. This seems reasonable, given the fact that the ionization cross section of CO_2 is higher than that of CO [48]. We consider the calibration constant for CO_2 to be more reliable though.

4.3. *Kinetics of CO oxidation at a porous electrode*

In this section, kinetic parameters of the dynamic 1D macrokinetic model for CO oxidation which was introduced in section 4.3 will be identified using the experimental data from the CO bulk oxidation experiment described in the previous section.

Overall, the assumption of a homogeneous boundary layer with only diffusive transport (compare section 3.2) seems reasonable for our experimental conditions. The diffusion boundary layer has about the same thickness as the velocity boundary layer for a Schmidt number of 1 and is smaller for Schmidt number larger than 1. In our case the Schmidt number (ν/D) is about 500. Thus, the diffusion boundary layer is a lot thinner than the velocity boundary layer and the assumption that there is no convective transport is reasonable. The thickness of the diffusion layer is approximately 0.1 mm whereas the electrode diameter is 10 mm - since diffusive transport is proportional to the concentration gradient we are making only a small mistake by neglecting the transport in other directions.

In total, eight parameters were fitted to the experimental data. A genetic algorithm starting with a set of randomly selected initial parameters is employed for finding the parameters that yield the best fit of experimental data and simulation results. The resulting parameter values can be found in Table 1. In six runs the genetic algorithm, which started from a different set of randomly chosen parameter values each time, converged at very similar parameter values (standard deviation of 11 % on average). While this does not guarantee that there is only one set of parameters from a mathematical point of view, it shows that the fitting procedure is quite robust despite of the high number of parameters. While in this work we aim at establishing the method, we do acknowledge

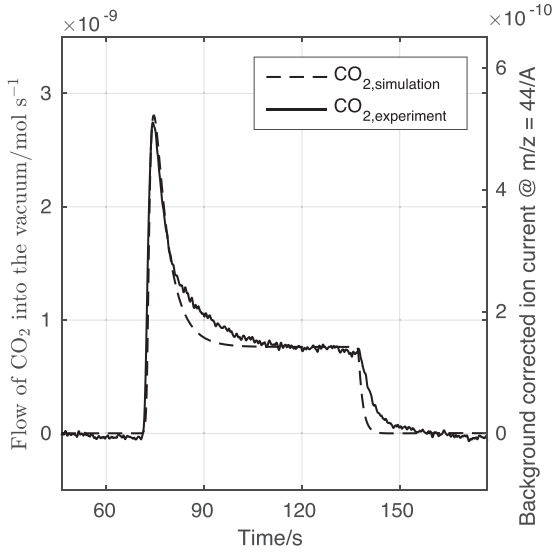

Fig. 9. Simulated and measured CO_2 flow into the vacuum system over time during CO bulk oxidation. The potential is stepped from 0.45 V to 0.65 V at $t = 72$s and back to 0.45 V at $t = 137$s at a flow rate of 430 ml/min for the CO-saturated electrolyte containing 0.25 mol/L $HClO_4$

that a systematic experimental study would increase the reliability of the results of the CO oxidation kinetics.

In Figs. 9 and 10, the measured and simulated current as well as the measured and simulated flow of CO_2 into the vacuum system over time are depicted for a positive potential step from 0.45 V to 0.65 V at $t = 72$s and a negative potential step back to 0.45 V at $t = 137$s. The simulated flow of CO_2 from the membrane into the vacuum system is calculated according to equation (24). The measured flow of CO_2 is calculated from the background corrected ion-current signal at m/z = 44, which can be read directly on the right y-axis, multiplied with the calibration constant according to equation (35).

The current signal peaks almost instantly after the potential step whereas the CO_2 signal rises quickly and peaks after 4.2 seconds in both experiment and simulation. The relation between mass

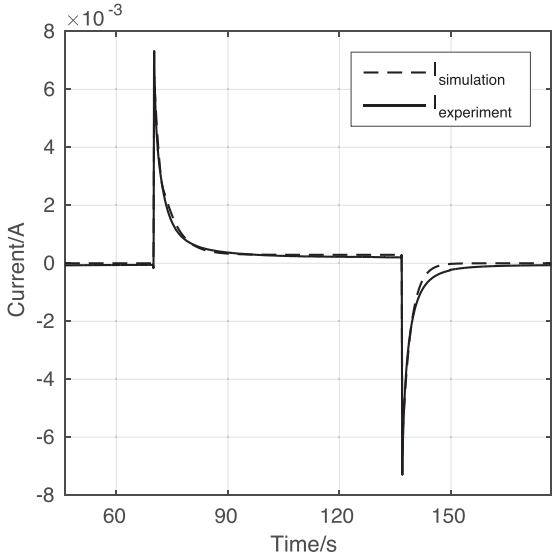

Fig. 10. Simulated and measured current over time during CO bulk oxidation. The potential is stepped from 0.45 V to 0.65 V at $t = 72$s and back to 0.45 V at $t = 137$s at a flow rate of 430 ml/min for the CO-saturated electrolyte containing 0.25 mol/L $HClO_4$

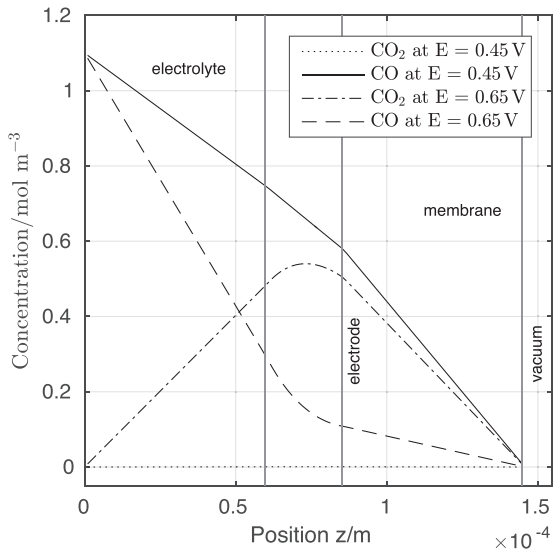

Fig. 11. Simulated steady state concentration profile of CO and CO_2 in the boundary layer (left), the electrode (middle) and the membrane (right) over the position at 0.45 and 0.65 V

spectrometer signal and CO_2 reaction rate that can be expressed as the calibration constant K for steady state conditions does not hold then because of transport effects and double layer charging. Subsequently, the curve falls and stabilizes at approximately $7 \cdot 10^{-10}$ mol/s. A small but steady decay of current and CO_2 flow into the vacuum can be observed in the experimental curves. This behavior has been observed before for platinum based catalysts and has been attributed to anion adsorption [49]. After the positive potential step the MS-signal increases quickly whereas it drops slightly slower after the negative potential step. The slow decay is mainly caused by diffusion of carbon dioxide in electrolyte, catalyst, and membrane. Overall there is a close agreement of the simulation results and the experimental data.

From the simulation results, not only kinetic parameters can be estimated. The concentration profiles and local reaction rates can be accessed and give further insight into the interaction of transport and reaction processes: In Fig. 11, the steady state concentration profile of CO and CO_2 in the boundary layer, the electrode and the membrane is depicted as a function of the z-coordinate for high and low potential. It can be seen that at low potential the concentration of CO is declining from the bulk value at the outer boundary layer to zero at the membrane-vacuum interface while there is no CO_2 present. During the oxidation at a potential of 0.65 V, the CO_2 that is produced in the electrode is diffusing through the membrane into the vacuum and through the boundary layer into the bulk where the concentration approaches zero. The CO concentration drops over the electrode, leading to the local reaction rate being only half as large at the membrane side of the electrode as on the electrolyte side.

Because of the initially high CO concentration and the high CO surface coverage in the electrode, the reaction rate increases sharply and exceeds the steady state value after a positive potential step. This is causing the CO_2 signal to overshoot as depicted in Fig. 9. The diffusion through the membrane causes a slight delay of the CO_2 signal compared to the current signal. On the other hand, after a negative potential step, the CO_2 which diffuses from the concentration boundary layer and the electrode through the membrane into the vacuum leads to a delayed decay of the amount of CO_2 entering the vacuum. There is a slight difference between simulation and experiment after the negative potential step. Three phenomena contribute to this deviation: Firstly, the limited speed of the vacuum pumps might cause some tailing of the signal. Secondly, our model underestimates the thickness of the concentration boundary layer in the middle of the electrode. From there CO_2 produced at high potential might diffuse back to the electrode for a longer period of time than predicted by the model. Finally, local CO_2 concentrations might exceed the solubility during CO oxidation at high potential, causing transport phenomena which we did not include in our model.

Additionally, we estimated the collection efficiency of the cyclone cell in steady state at different flow rates by changing the thickness of the diffusion layer in the model and calculating N: Increasing the flow rate to 600 ml/min leads to a predicted value of N = 0.5. Decreasing the flow rate to 300 ml/ min results in a collection efficiency of approximately 0.75, decreasing it further to 200 ml/min in N = 0.85.

In conclusion, the model is capable of giving an insight into the dynamic transport and reaction processes and their interaction inside a porous DEMS electrode. Parameter identification using the online CO_2 measurement from the DEMS in combination with current and potential has advantages over using current and potential only. Effects such as double layer capacitance and anion adsorption are difficult to separate from the reaction currents by monitoring current and potential alone but they do not influence the direct online detection of reaction products by DEMS.

5. Conclusions

A new cyclone flow DEMS cell for analyzing products of electrochemical reactions inside porous electrodes online has been presented. The designed cyclone cell features a homogeneous concentration profile over 75% of the electrode area, a simple design without any moving parts, defined convection and high collection efficiency. The disadvantages of classical DEMS cells such as badly defined mass transfer and locally varying concentrations are circumvented. Though the CFD simulations of the mass transfer are sufficient for the purpose of the current study it would certainly be interesting to resolve the deviation to the literature values which we discussed. We would like to point out that the comparatively high flow rates required by the cyclone flow cell are a disadvantage because they restrict the use of expensive reactants and make long term experiments difficult. The second point is less severe in our opinion considering the fact that the cell is designed for examining fast processes rather than for undertaking long term studies. We demonstrated a methodology how to combine DEMS experiments, flow analysis and physical modeling to gain quantitative understanding of processes inside porous electrodes. The model based description of the electrode processes allows reliable parameter identification and simultaneous analysis of electrode transport properties and electrochemical properties. While the well-researched example of CO oxidation served as an example to establish the methodology we expect that this setup and approach will be useful for analyzing kinetics of different kinds of reaction on porous electrodes and expand the scope of DEMS to help modeling kinetics quantitatively and reliably.

Acknowledgements

We would like to thank Tanja Vidaković -Koch for fruitful discussions about the cyclone cell, Peter Bogdanoff for his support in setting up the DEMS, and the group of Helmut Baltruschat for valuable advice on conducting DEMS experiments.

Appendix A.

A.1. Levich-type equation for the DEMS cyclone flow cell

The Levich equation which can be expressed in dimensionless numbers as $Sh = 0.62 Re^{1/2} Sc^{1/3}$ is usually applied in electrochemistry to calculate diffusion limited current densities in the following form:

$$i_{\mathrm{lim}} = 0.62 z F D^{2/3} \omega^{1/2} \nu^{-1/6} c_{\infty} \tag{37}$$

Accordingly, the mass transfer relationship for the constructed DEMS cyclone flow cell could be rewritten in the shape of a Levich-type relationship by re-substituting the dimensionless numbers in equation (31), yielding:

$$i_{\mathrm{lim}} = 0.021 z F D^{2/3} \left(\frac{4 \dot{V} R_{\mathrm{in}}^{1/2}}{\pi d_{\mathrm{in}}^2 R_{\mathrm{el}}} \right)^{2/3} \nu^{-1/3} c_{\infty} \tag{38}$$

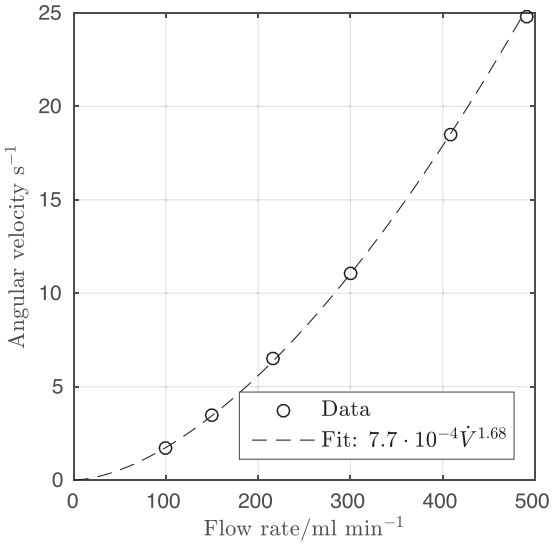

Fig. 12. Simulated average angular velocity at $r = R_{\mathrm{el}}$ for different flow rates

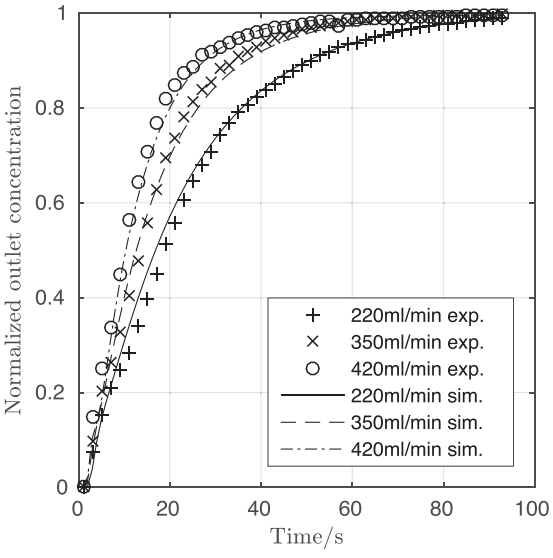

Fig. 13. Simulated and measured residence time distribution curves at different flow rates

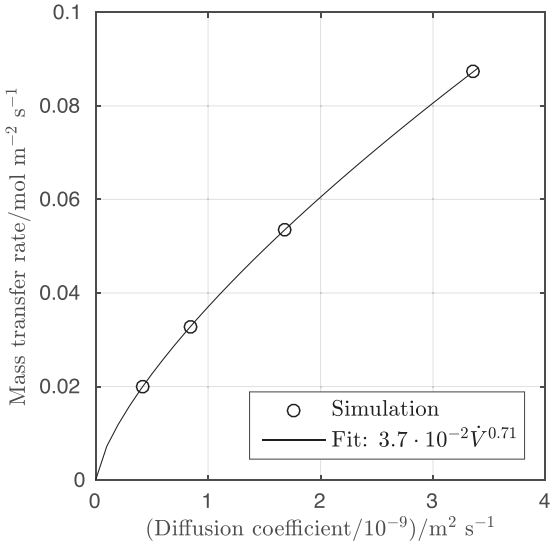

Fig. 14. Simulated mass transfer rate over diffusion coefficient at a flow rate of 216 ml/min

References

[1] O. Wolter, J. Heitbaum, Differential Electrochemical Mass Spectroscopy (DEMS) - a new method for the study of electrode processes, Berichte der Bunsengesellschaft für Physikalische Chemie 88 (1) (1984) 2–6.

[2] M. Fujihira, T. Noguchi, A novel differential electrochemical mass spectrometer (DEMS) with a stationary gas-permeable electrode in a rotational flow produced by a rotating rod, Journal of Electroanalytical Chemistry 347 (1993) 457–463.

[3] S. Wasmus, E. Cattaneo, W. Vielstich, Reduction of carbon dioxide to methane and ethene - an on-line MS study with rotating electrodes, Electrochimica Acta 35 (4) (1990) 771–775.

[4] D. Tegtmeyer, J. Heitbaum, A. Heindrichs, Electrochemical on line mass spectrometry on a rotating electrode inlet system, Berichte der Bunsengesellschaft für Physikalische Chemie 93 (2) (1989) 201–206.

[5] I. Treufeld, A.J.J. Jebaraj, J. Xu, D. Martins de Godoi, D. Scherson, Porous Teflon ring-solid disk electrode arrangement for differential mass spectrometry measurements in the presence of convective flow generated by a jet impinging electrode in the wall-jet configuration, Analytical Chemistry 84 (12) (2012) 5175–5179.

[6] T. Hartung, H. Baltruschat, Differential electrochemical mass spectrometry using smooth electrodes: adsorption and hydrogen/deuterium exchange reactions of benzene on platinum, Langmuir 6 (5) (1990) 953–957.

[7] T. Hartung, U. Schmiemann, I. Kamphausen, H. Baltruschat, Electrodesorption from single-crystal electrodes: analysis by differential electrochemical mass spectrometry, Analytical Chemistry 63 (1) (1991) 44–48.

[8] Z. Jusys, H. Massong, H. Baltruschat, A new approach for simultaneous DEMS and EQCM: Electro-oxidation of adsorbed CO on Pt and Pt-Ru, Journal of The Electrochemical Society 146 (3) (1999) 1093–1098.

[9] H. Wang, T. Löffler, H. Baltruschat, Formation of intermediates during methanol oxidation: A quantitative DEMS study, Journal of Applied Electrochemistry 31 (7) (2001) 759–765.

[10] H. Wang, L.R. Alden, F.J. DiSalvo, H.D. Abruña, Methanol electrooxidation on PtRu bulk alloys and carbon-supported PtRu nanoparticle catalysts: a quantitative DEMS study, Langmuir 25 (13) (2009) 7725–7735.

[11] A.-E.-A.A. Abd-El-Latif, J. Xu, N. Bogolowski, P. Königshoven, H. Baltruschat, New Cell for DEMS Applicable to Different Electrode Sizes, Electrocatalysis 3 (1) (2011) 39–47.

[12] H. Wang, L. Alden, F.J. Disalvo, H.D. Abruña, Electrocatalytic mechanism and kinetics of SOMs oxidation on ordered PtPb and PtBi intermetallic compounds: DEMS and FTIRS study, Physical Chemistry Chemical Physics 10 (25) (2008) 3739–3751.

[13] H. Wang, E. Rus, H.D. Abruña, New double-band-electrode channel flow differential electrochemical mass spectrometry cell: application for detecting product formation during methanol electrooxidation., Analytical Chemistry 82 (11) (2010) 4319–4324.

[14] A. Wonders, T. Housmans, V. Rosca, M. Koper, On-line mass spectrometry system for measurements at single-crystal electrodes in hanging meniscus configuration, Journal of Applied Electrochemistry 36 (11) (2006) 1215–1221.

[15] Y. Gao, H. Tsuji, H. Hattori, H. Kita, New on-line mass spectrometer system designed for platinum-single crystal electrode and electroreduction of acetylene, Journal of Electroanalytical Chemistry 372 (1-2) (1994) 195–200.

[16] K. Jambunathan, A.C. Hillier, Measuring electrocatalytic activity on a local scale with scanning Differential Electrochemical Mass Spectrometry, Journal of The Electrochemical Society 150 (6) (2003) E312.

[17] S. Pérez-Rodríguez, M. Corengia, G. García, C.F. Zinola, M.J. Lázaro, E. Pastor, Gas diffusion electrodes for methanol electrooxidation studied by a new DEMS configuration: Influence of the diffusion layer, International Journal of Hydrogen Energy 37 (8) (2012) 7141–7151.
[18] J. Flórez-Montaño, G. García, J.L. Rodríguez, E. Pastor, P. Cappellari, G.A. Planes, On the design of Pt based catalysts. Combining porous architecture with surface modification by Sn for electrocatalytic activity enhancement, Journal of Power Sources 282 (2015) 34–44.
[19] C. Niether, M. Rau, C. Cremers, D. Jones, K. Pinkwart, J. Tübke, Development of a novel experimental DEMS set-up for electrocatalyst characterization under working conditions of high temperature polymer electrolyte fuel cells, Journal of Electroanalytical Chemistry 747 (2015) 97–103.
[20] T. Seiler, E. Savinova, K. Friedrich, U. Stimming, Poisoning of PtRu/C catalysts in the anode of a direct methanol fuel cell: a DEMS study, Electrochimica Acta 49 (22-23) (2004) 3927–3936.
[21] N. Anastasijevic, H. Baltruschat, J. Heitbaum, DEMS as a tool for the investigation of dynamic processes: galvanostatic formic acid oxidation on a Pt electrode, Journal of Electroanalytical Chemistry and Interfacial Electrochemistry 272 (1-2) (1989) 89–100.
[22] R. Schwiedernoch, S. Tischer, C. Correa, O. Deutschmann, Experimental and numerical study on the transient behavior of partial oxidation of methane in a catalytic monolith, Chemical Engineering Science 58 (3-6) (2003) 633–642.
[23] D. Zhang, O. Deutschmann, Y.E. Seidel, R.J. Behm, Interaction of mass transport and reaction kinetics during electrocatalytic co oxidation in a thin-layer flow cell, Journal of Physical Chemistry C 115 (2) (2011) 468–478.
[24] G.A. Planes, G. García, E. Pastor, High performance mesoporous Pt electrode for methanol electrooxidation. A DEMS study, Electrochemistry Communications 9 (4) (2007) 839–844.
[25] J. Fuhrmann, A. Linke, H. Langmach, H. Baltruschat, Numerical calculation of the limiting current for a cylindrical thin layer flow cell, Electrochimica Acta 55 (2) (2009) 430–438.
[26] T. Chuah, J. Gimbun, T.S. Choong, A CFD study of the effect of cone dimensions on sampling aerocyclones performance and hydrodynamics, Powder Technology 162 (2) (2006) 126–132.
[27] M. Heinen, Y.X. Chen, Z. Jusys, R.J. Behm, Room temperature COad desorption/exchange kinetics on Pt electrodes - A combined in situ ir and mass spectrometry study, ChemPhysChem 8 (17) (2007) 2484–2489.
[28] T. Iwasita, U. Vogel, Interaction of methanol and CO adsorbate on platinum with CH3OH and CO in solution, Electrochimica Acta 33 (4) (1988) 557–560.
[29] B. Geng, J. Cai, S.X. Liu, P. Zhang, Z.Q. Tang, D. Chen, Q. Tao, Y.X. Chen, S.Z. Zou, Temperature programmed Desorption - An application to kinetic studies of CO desorption at electrochemical interfaces, Journal of Physical Chemistry C 113 (47) (2009) 20152–20155.
[30] H. Baltruschat, Differential electrochemical mass spectrometry, Journal of the American Society for Mass Spectrometry 15 (12) (2004) 1693–1706.
[31] T. Vidaković, M. Christov, K. Sundmacher, Investigation of electrochemical oxidation of methanol in a cyclone flow cell, Electrochimica Acta 49 (13) (2004) 2179–2187.
[32] H. Uchida, K. Izumi, M. Watanabe, Temperature Dependence of CO-Tolerant Hydrogen Oxidation Reaction Activity at Pt, Pt-Co, and Pt-Ru Electrodes, The Journal of Physical Chemistry B 110 (43) (2006) 21924–21930.
[33] E.L. Cussler, Diffusion: Mass transfer in fluid systems, 2nd Edition, Cambridge University Press, New York, 1997.
[34] A.J. Bard, L.R. Faulkner, Electrochemical Methods Fundamentals and Applications, 2nd Edition, John Wiley & Sons, Inc., New York, 2001.
[35] K. Sundmacher, Cyclone Flow cell for the investigation of gas-diffusion electrodes, Journal of Applied Electrochemistry 29 (1999) 919–926.
[36] U.T. Bödewadt, Die Drehströmung über festem Grunde, ZAMM - Zeitschrift für Angewandte Mathematik und Mechanik 20 (5) (1940) 241–253.
[37] J. E. Nydahl, Heat Transfer for the Bödewadt Problem, Tech. rep., Colorado State University, Fort Collins, CO. (1971).
[38] W.J. Albery, S. Bruckenstein, Uniformly accessible electrodes, Journal of Electroanalytical Chemistry and Interfacial Electrochemistry 144 (1-2) (1983) 105–112.
[39] M. Bergelin, M. Wasberg, The impinging jet flow method in interfacial electrochemistry: an application to bead-type electrodes, Journal of Electroanalytical Chemistry 449 (1-2) (1998) 181–191.
[40] M. Bergelin, E. Herrero, J.M. Feliu, M. Wasberg, Oxidation of CO adlayers on Pt(111) at low potentials: an impinging jet study in H2SO4 electrolyte with mathematical modeling of the current transients, Journal of Electroanalytical Chemistry 467 (1) (1999) 74–84.
[41] J.J. Carroll, J.D. Slupsky, A.E. Mather, The solubility of carbon dioxide in water at low pressure, Journal of Physical and Chemical Reference Data 20 (6) (1991) 1201.
[42] C.J. Bondue, A.-E.-A.A. Abd-El-Latif, P. Hegemann, H. Baltruschat, Quantitative Study for Oxygen Reduction and Evolution in Aprotic Organic Electrolytes at Gas Diffusion Electrodes by DEMS, Journal of The Electrochemical Society 162 (3) (2015) 479–487.
[43] M. Khodayari, P. Reinsberg, A.-E.-A.A. Abd-El-Latif, C. Merdon, J. Fuhrmann, H. Baltruschat, Determining solubility and diffusivity using a flow cell coupled to mass spectrometer, ChemPhysChem (2016).
[44] T. Vidaković, M. Christov, K. Sundmacher, A method for rough estimation of the catalyst surface area in a fuel cell, Journal of Applied Electrochemistry 39 (2) (2009) 213–225.
[45] M.S. Masdar, T. Tsujiguchi, N. Nakagawa, Mass spectroscopy for the anode gas layer in a semi-passive DMFC using porous carbon plate Part I: Relationship between the gas composition and the current density, Journal of Power Sources 194 (2) (2009) 610–617.
[46] J. Willsau, J. Heitbaum, The influence of Pt-activation on the corrosion of carbon in gas diffusion electrodes - a DEMS study, Journal of Electroanalytical Chemistry and Interfacial Electrochemistry 161 (1) (1984) 93–101.
[47] Mass Spectroscopy Soc. of Japan, MassBank Record: JP001576 (2011).
[48] P.J. Linstrom, W. Mallard (Eds.), NIST Chemistry WebBook, NIST Standard Reference Database Number 69, National Institute of Standards and Technology, Gaithersburg, 2016.
[49] E. Mostafa, A.-E.-A.A. Abd-El-Latif, H. Baltruschat, Electrocatalytic Oxidation and Adsorption Rate of Methanol at Pt Stepped Single-Crystal Electrodes and Effect of Ru Step Decoration: A DEMS Study, ChemPhysChem 15 (10) (2014) 2029–2043.